A&A 604, A135 (2017)
DOI: 10.1051/0004-6361/201730986

Astronomy & Astrophysics

The *Gaia*-ESO Survey: dynamics of ionized and neutral gas in the Lagoon nebula (M 8)[⋆,⋆⋆]

F. Damiani[1], R. Bonito[1,2], L. Prisinzano[1], T. Zwitter[3], A. Bayo[4], V. Kalari[5], F. M. Jiménez-Esteban[6], M. T. Costado[7], P. Jofré[8,9], S. Randich[10], E. Flaccomio[1], A. C. Lanzafame[11], C. Lardo[12], L. Morbidelli[10], and S. Zaggia[13]

[1] INAF – Osservatorio Astronomico di Palermo G. S. Vaiana, Piazza del Parlamento 1, 90134 Palermo, Italy
e-mail: `damiani@astropa.inaf.it`
[2] Dipartimento di Fisica e Chimica, Università di Palermo, Piazza del Parlamento 1, 90134 Palermo, Italy
[3] Faculty of Mathematics and Physics, University of Ljubljana, Jadranska 19, 1000 Ljubljana, Slovenia
[4] Instituto de Física y Astronomía, Universidad de Valparaíso, Chile
[5] Departamento de Astronomía, Universidad de Chile, Casilla 36-D Santiago, Chile
[6] Departamento de Astrofísica, Centro de Astrobiología (INTA-CSIC), ESAC Campus, Camino Bajo del Castillo s/n, 28692 Villanueva de la Cañada, Madrid, Spain
[7] Instituto de Astrofísica de Andalucía-CSIC, Apdo. 3004, 18080 Granada, Spain
[8] Institute of Astronomy, University of Cambridge, Madingley Road, Cambridge CB3 0HA, UK
[9] Núcleo de Astronomía, Facultad de Ingeniería, Universidad Diego Portales, Av. Ejército 441, Santiago, Chile
[10] INAF – Osservatorio Astrofisico di Arcetri, Largo E. Fermi 5, 50125 Florence, Italy
[11] Dipartimento di Fisica e Astronomia, Sezione Astrofisica, Università di Catania, via S. Sofia 78, 95123 Catania, Italy
[12] Laboratoire d'Astrophysique, École Polytechnique Fédérale de Lausanne (EPFL), Observatoire de Sauverny, 1290 Versoix, Switzerland
[13] INAF – Padova Observatory, Vicolo dell'Osservatorio 5, 35122 Padova, Italy

Received 13 April 2017 / Accepted 23 May 2017

ABSTRACT

Aims. We present a spectroscopic study of the dynamics of the ionized and neutral gas throughout the Lagoon nebula (M 8), using VLT-FLAMES data from the *Gaia*-ESO Survey. The new data permit exploration of the physical connections between the nebular gas and the stellar population of the associated star cluster NGC 6530.

Methods. We characterized through spectral fitting emission lines of Hα, [N II] and [S II] doublets, [O III], and absorption lines of sodium D doublet, using data from the FLAMES-Giraffe and UVES spectrographs, on more than 1000 sightlines toward the entire face of the Lagoon nebula. Gas temperatures are derived from line-width comparisons, densities from the [S II] doublet ratio, and ionization parameter from Hα/[N II] ratio. Although doubly-peaked emission profiles are rarely found, line asymmetries often imply multiple velocity components along the same line of sight. This is especially true for the sodium absorption, and for the [O III] lines.

Results. Spatial maps for density and ionization are derived, and compared to other known properties of the nebula and of its massive stars 9 Sgr, Herschel 36 and HD 165052 which are confirmed to provide most of the ionizing flux. The detailed velocity fields across the nebula show several expanding shells, related to the cluster NGC 6530, the O stars 9 Sgr and Herschel 36, and the massive protostar M 8East-IR. The origins of kinematical expansion and ionization of the NGC 6530 shell appear to be different. We are able to put constrains on the line-of-sight (relative or absolute) distances between some of these objects and the molecular cloud. The data show that the large obscuring band running through the middle of the nebula is being compressed by both sides, which might explain its enhanced density. We also find an unexplained large-scale velocity gradient across the entire nebula. At larger distances, the transition from ionized to neutral gas is studied using the sodium lines.

Key words. ISM: individual objects: Lagoon nebula – ISM: general – HII regions

1. Introduction

The Lagoon nebula (M 8, NGC 6523) is one of the brightest H_{II} regions in the solar neighborhood, and has been the subject of many observational studies (e.g., Lada et al. 1976, in CO and optical lines; Tothill et al. 2002, in CO and sub-mm; Takeuchi et al. 2010, in CO). It harbors the young cluster NGC 6530, only a few Myrs old, and also intensively studied especially in recent years at optical, infrared and X-ray wavelengths (e.g., Walker 1957; van den Ancker et al. 1997; Sung et al. 2000; Damiani et al. 2004, 2006; Prisinzano et al. 2005, 2007; Kumar & Anandarao 2010; Povich et al. 2013). The H_{II} region is illuminated by many massive stars of O and B spectral types, the hottest one being 9 Sgr (HD 164794, type O4V((f))z); a few other late-O or B type stars are also found in the region. The optically brightest part of the Lagoon nebula is the so-called Hourglass nebula, which surrounds and partially oscures the O7:V star Herschel 36 (Woodward et al. 1986); stars in the Hourglass are thought to be younger than the NGC 6530 cluster. Also noteworthy is the presence, to the east of NGC 6530, of

---

[⋆] Based on observations collected with the FLAMES spectrograph at VLT/UT2 telescope (Paranal Observatory, ESO, Chile), for the *Gaia*-ESO Large Public Survey (program 188.B-3002).

[⋆⋆] Full Tables A.1 and A.2 are only available at the CDS via anonymous ftp to `cdsarc.u-strasbg.fr` (`130.79.128.5`) or via `http://cdsarc.u-strasbg.fr/viz-bin/qcat?J/A+A/604/A135`

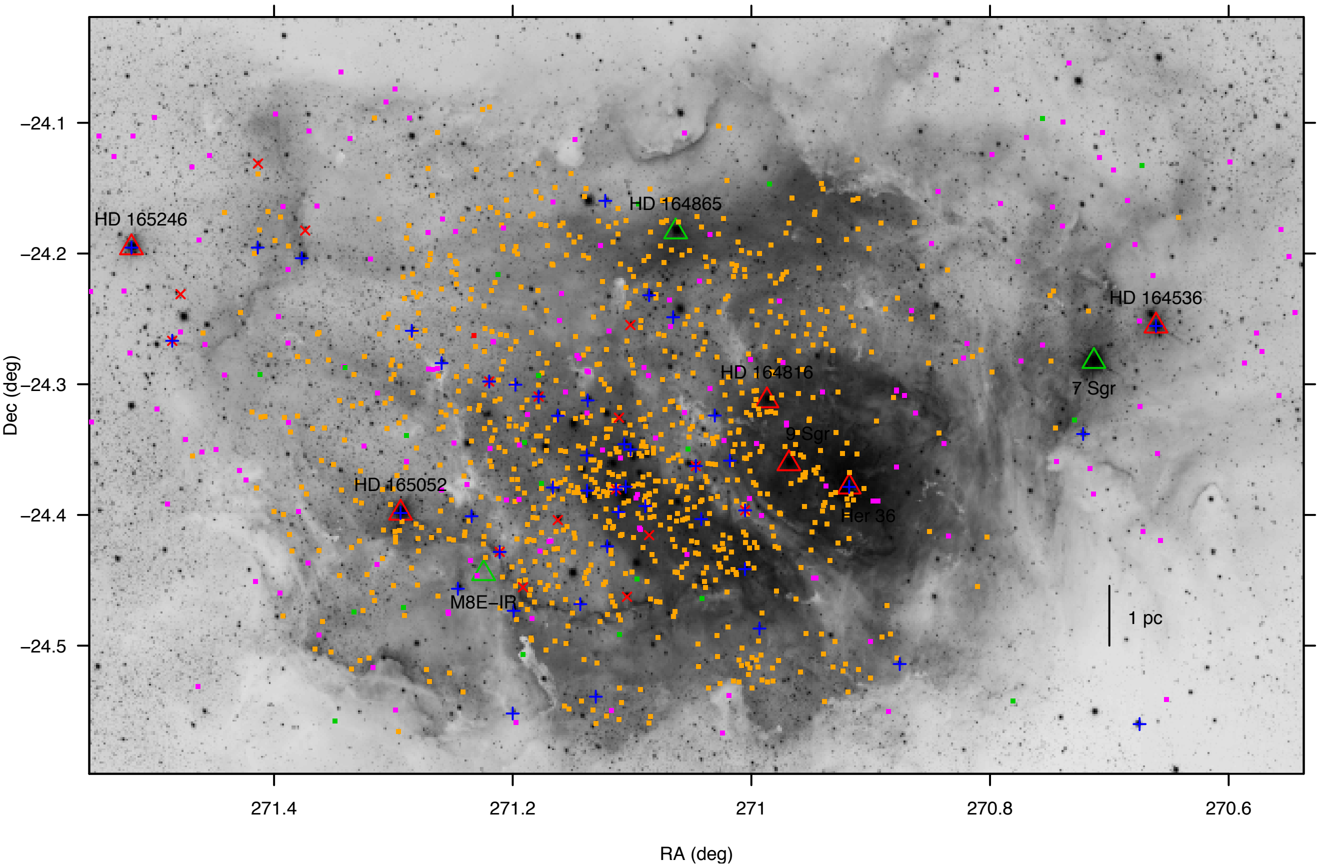

Fig. 1. VPHAS+ image of the Lagoon nebula (size 55.8′ × 34.8′, corresponding to 20.36 × 12.7 pc), with superimposed all *Gaia*-ESO target positions used in this work. Giraffe targets are indicated with magenta (sky fibres) or orange (faint stars) filled squares. UVES sky fibres are indicated with red (setup 580) or green (setup 520) filled squares. Only one UVES-580 sky fibre position is not coincident with (and its symbol not hidden by) an UVES-520 sky fibre position. UVES stars are indicated with red crosses (setup 580) or blue "+" signs (setup 520). Red triangles indicate the O stars HD 165246, HD 165052, HD 164816, 9 Sgr, Herschel 36, and HD 164536. Green triangles indicate the massive objects M 8E-IR, HD 164865, and 7 Sgr. North is up and east to the left.

the embedded massive protostar M 8E-IR (Wright et al. 1977; Simon et al. 1984; Henning & Gürtler 1986), indicating that star formation in the region has also taken place recently. The most recent determination of the distance of the NGC 6530 cluster (and by inference of the H_{II} region as well) is 1250 pc (Prisinzano et al. 2005). The properties of the whole region were reviewed by Tothill et al. (2008).

The Lagoon nebula and its stellar population show a well-defined spatial organization. The brightest nebular region (Hourglass) does not lie near the geometrical center of the whole nebula, but several arcmin (~2 pc) to the west. Closer to the nebula center lies instead the bulk of low-mass cluster stars (Damiani et al. 2004), cospatial with the B stars. The most massive member 9 Sgr is also offset with respect to the B stars, but appears not directly related to any localized bright nebulosity, leading Lada et al. (1976) to suggest that it actually lies several parsecs in front of the nebula, not within it. All around the central region, many bright-rimmed dark clouds are found, which being located along the outer border of the nebula suggest the blister nature of the H_{II} region. Behind one of them to the south-east of the main cluster, the mentioned young, massive star M 8E-IR is found. This and other low-mass stars in the same neighborhood show indications of being younger than the main NGC 6530 cluster (Damiani et al. 2004). The bright Hourglass region has received much more attention than the outer nebula parts, which remain relatively little studied.

In this work we studied the kinematics of the ionized and neutral gas giving rise to the strong optical emission lines (Hα, [N II], [S II], [O III]), and sodium D absorption lines, across the whole nebula, using new spectroscopic data from the *Gaia*-ESO Survey (Gilmore et al. 2012; Randich et al. 2013). In Sect. 2 we describe the observations, while in Sect. 3 we present our results. In Sect. 4 we discuss the main implications of our work for the structure and dynamics of the Lagoon nebula, including issues that deserve further research.

2. Observational data

The observations of the Lagoon nebula were obtained as part of the *Gaia*-ESO Survey (internal release *iDR4*), targeting Milky Way stars and clusters across a wide range of parameters with the ESO VLT-FLAMES multi-fibre spectrograph (Pasquini et al. 2002). Twenty-seven observing blocks (OBs) were devoted to NGC 6530 as part of the Survey program, down to a limiting stellar magnitude $V = 19$. Observations were spread over 17 nights, in September 2012 and June–September 2013. Fifteen fibres per OB were targeted at star-free sky positions, interspersed between stellar position, with the intent of obtaining purely nebular spectra needed to correct the stellar spectra through subtraction. Spectrographs used were Giraffe (setup HR15N, $R \sim 19\,000$, wavelength range 6444–6818 Å) and UVES (setup 580, $R \sim 47\,000$, range 4768–6830 Å; and setup 520, $R \sim 47\,000$, range

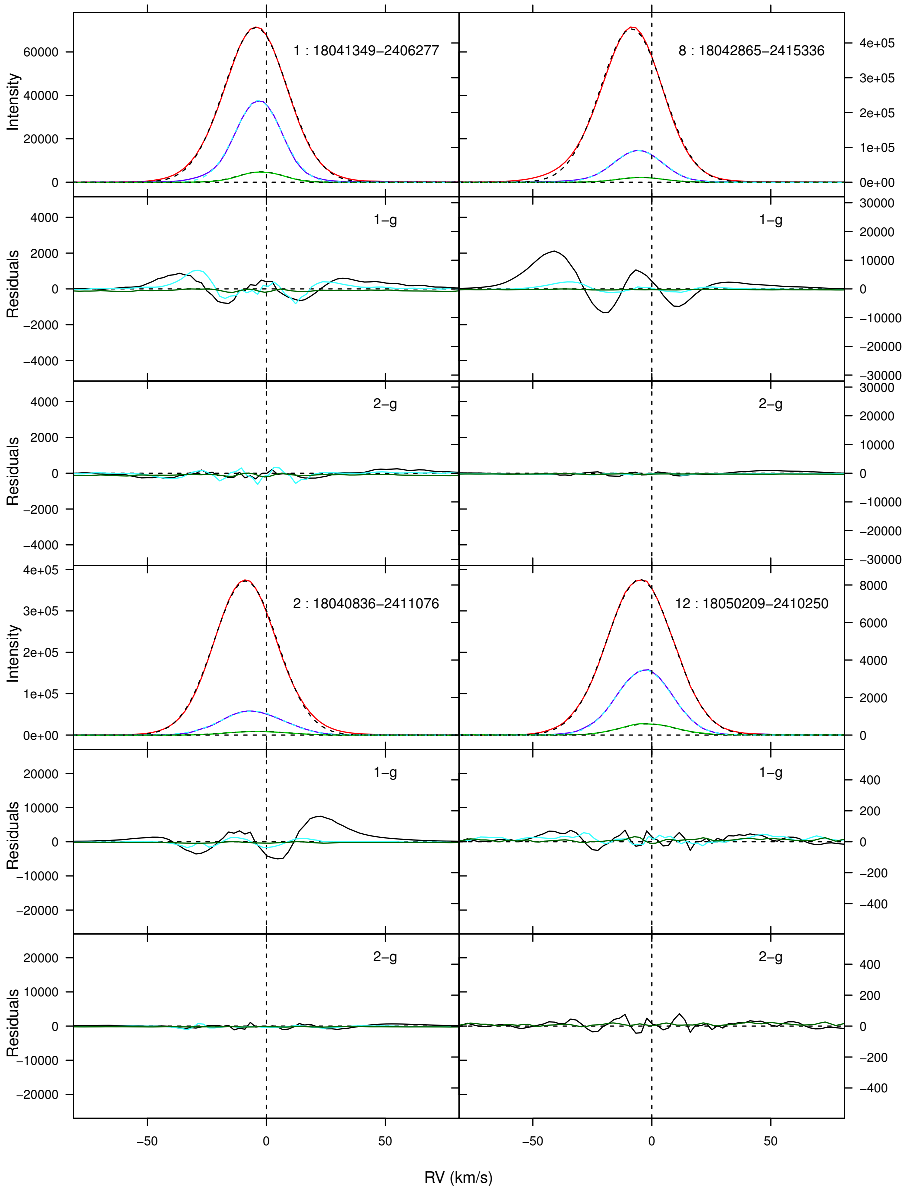

Fig. 2. Four examples of nebular line profiles of Hα (red), [N II] 6584 (blue), and [S II] 6731 (green) lines, and their best-fit models using both one- and two-Gaussian models (black, cyan and dark-green dashed lines, for Hα, [N II] and [S II] respectively). The ordinate scale is the same for all lines. Only pure-sky spectra from Giraffe are shown. *Each panel labeled with sky position* shows the observed spectrum with superimposed the one-Gaussian best-fit model for each line. Below it, the fit residuals (labeled "1-g") for the one-Gaussian model are shown, with an ordinate scale enlarged 15 times; still below, the fit residuals for the two-Gaussian model (labeled "2-g") are shown on the same scale.

4180–6212 Å). The number of sky spectra obtained with Giraffe is 647 (on 197 individual sky positions), four spectra with UVES setup 580 (three positions), and 25 spectra with UVES setup 520 (21 positions). In addition, being so bright, the nebula dominates clearly the stellar spectra of faint stars, and the strongest nebular lines could be studied with good results whenever the ratio between Hα peak and stellar continuum is larger than 100 (henceforth "faint stars"), so that the Hα line cannot be dominated by the star, even in strongly accreting T Tauri stars. The same method was successfully used by us in a previous work on the emission of the Carina nebula using *Gaia*-ESO data (Damiani et al. 2016). The number of faint star spectra in the NGC 6530 *Gaia*-ESO dataset is 980 (892 individual stars, with some having been observed more than once). Therefore, only considering Giraffe spectra, we have nebular spectra for 1089 positions across the Lagoon nebula. The Giraffe HR15N wavelength range includes several strong nebular lines: Hα, the neighboring [N II] lines at 6548, 6584 Å, and the two [S II] lines at 6716, 6731 Å. Also the He I line at 6678 Å falls in the range, but is found to be too weak in our spectra for a proper study. Spectra for the same sky position were coadded to improve the S/N ratio. All the studied nebular lines are orders of magnitude stronger than atmospheric lines, as estimated from other *Gaia*-ESO spectra in clusters free of nebulosity.

The UVES sky spectra are very few as mentioned, and add little information despite the much wider wavelength range; they are therefore not considered further. On the other hand, the UVES spectra of stellar targets in NGC 6530 are more numerous (16 stars using setup 580, and 44 using setup 520, mostly of early type), and were used to study two important lines: the [O III] line at 5007 Å, clearly detected in most spectra, and the Na I D1, D2 absorption lines at 5895.92, 5889.95 Å. The latter enabled us to perform a comparative study of the ionized and the neutral gas in the region. Like the ionic lines, also these sodium absorption lines are much stronger than typical atmospheric sodium absorption. An Hα image of the Lagoon nebula from the VPHAS+ survey (Drew et al. 2014) is shown in Fig. 1, together with all sky positions considered here, and positions of several of the most massive stars.

Since the exposure times (20–50 min) were determined by the requirements dictated by the faintest stars, the signal-to-noise ratio (S/N) in the main nebular lines is usually very high (but

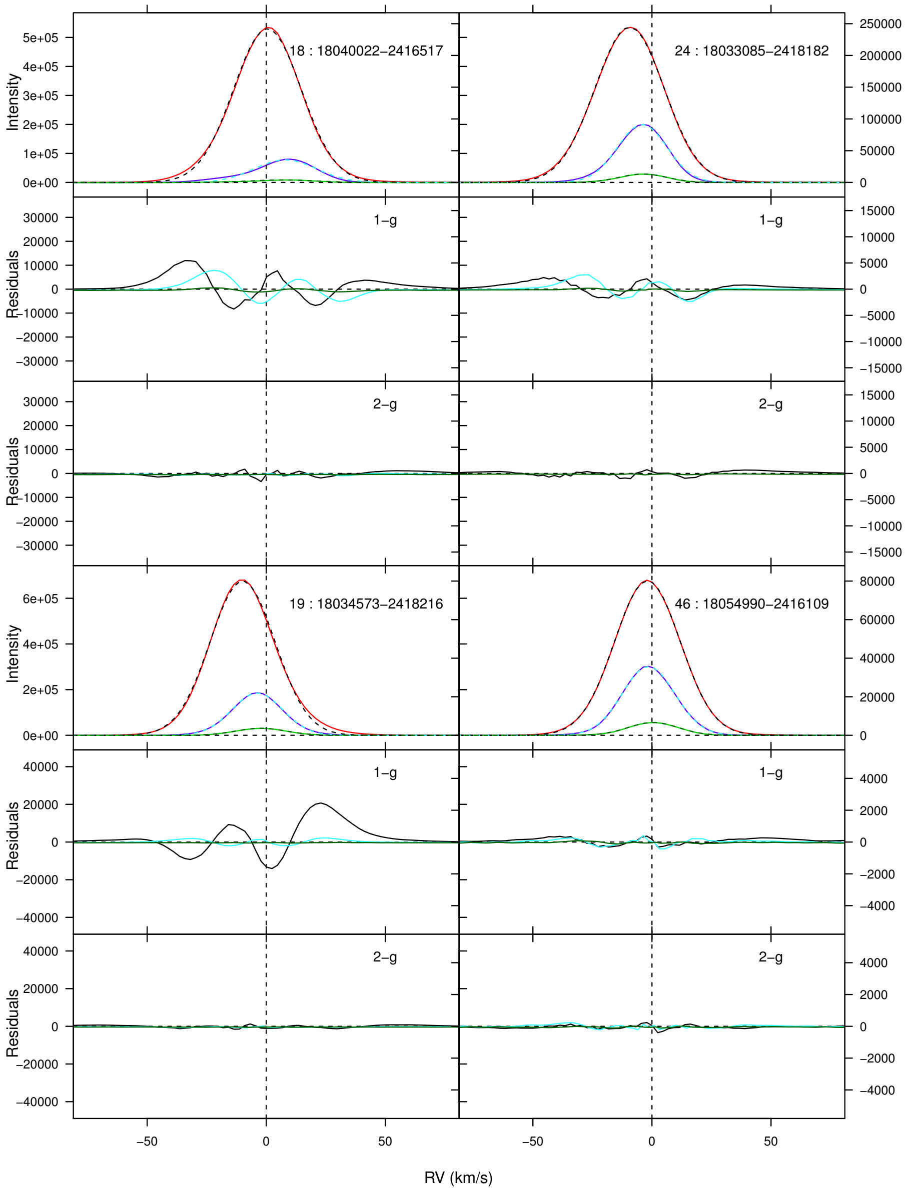

Fig. 3. Additional examples of observed line profiles and their best-fit models, as in Fig. 2, showing large differences between the peak radial velocities of Hα and [N II], and occasional asymmetrical residuals.

lines remain unsaturated). The high S/N and the large number of nebular positions comprised in our dataset make it one of the richest datasets ever available for the study being performed.

3. Results

3.1. Hα, [N II] and [S II] lines from Giraffe data

In order to study the dynamics of the nebular gas the optical emission lines were analyzed and modeled with analytical functions, starting with lines from Giraffe spectra. Figures 2 to 4 show several examples of the observed lines of Hα, [N II] 6584 Å, and [S II] 6731 Å (panels labeled with coordinates), and the residuals after subtraction of single-Gaussian (panels labeled with 1-g) or double-Gaussian (labeled 2-g) best-fit models. In nearly all cases the optical lines were found single-peaked: among all 197 pure-sky fibres only two cases of doubly-peaked lines were found (Fig. 4, right panels), and only in the [N II] and [S II] lines while not in Hα. In general, lines were found to be nearly Gaussian in shape, suggesting a single kinematical component along each line of sight for each emitting ion, as the representative examples of Figs. 2 and 3 show. However, while a single Gaussian (henceforth 1-g model) accounted well for the bulk of the emission in each line, examination of the fitting residuals (panels labeled 1-g) revealed that the detailed line shape was systematically misreproduced by a simple Gaussian function, by a small but significant amount in terms of the available S/N (we note that the ordinate scale in each of the 1-g residuals panels is 1/15 that of the panel above it). The systematic pattern of the 1-g model residuals was suggestive of at least two unresolved velocity components along the same sightline; only in rare cases the 1-g residuals showed no such pattern (Fig. 2, spectrum #12). In order to model the line profiles in detail, double-Gaussian (2-g) models were therefore attempted, whose residuals are also shown in Figs. 2–4 (panels labeled 2-g): these showed in nearly all cases no systematic patterns, indicating that two Gaussian components provide a sufficient characterization of emission lines in the Lagoon nebula. It should be remarked that each emission line (Hα, [N II] 6584 and [S II] 6717, 6731 Å) was fit independently; as the first three panels of Fig. 3 show particularly well, the Hα emission peak may lie at velocities significantly different than the peaks of [N II] and

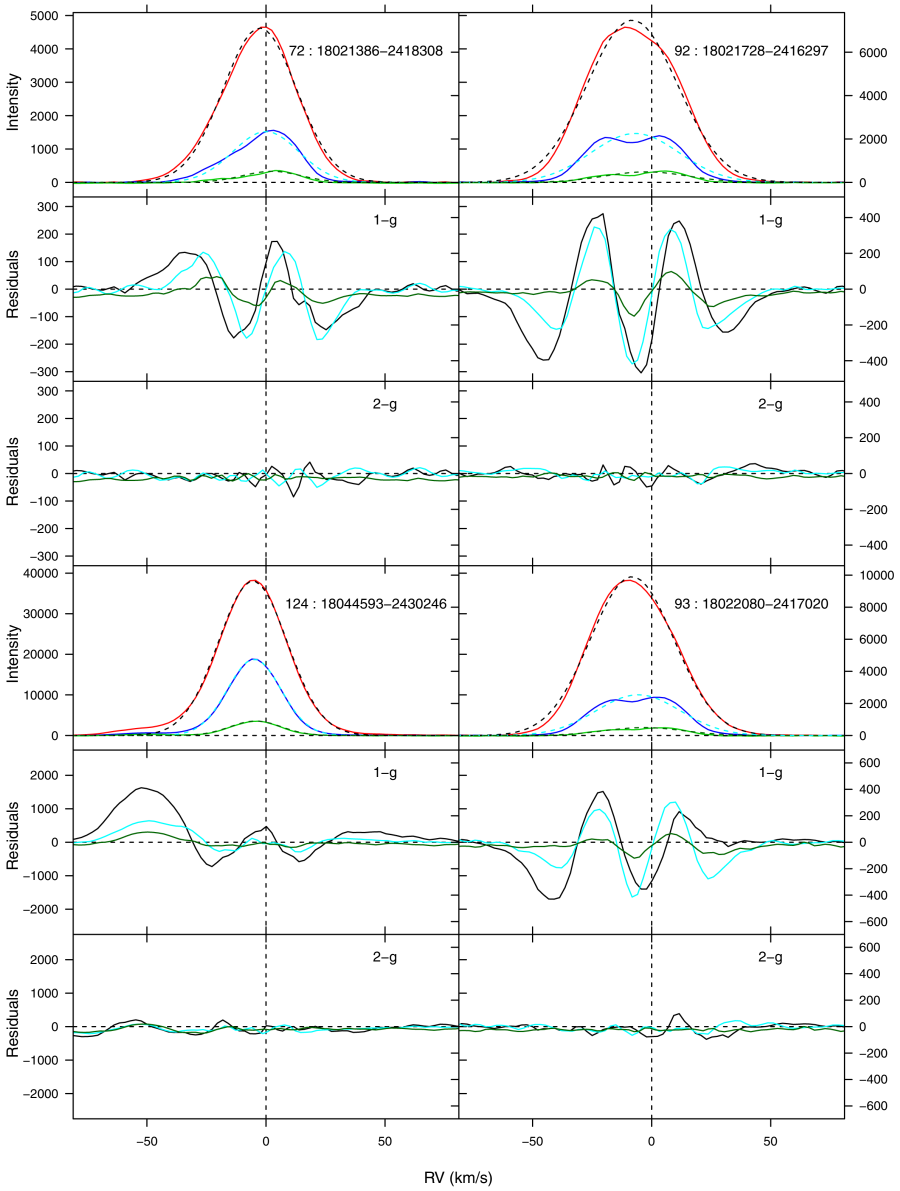

Fig. 4. Additional examples of observed line profiles and their best-fit models, as in Fig. 2. Here we show line profiles with the most evident distortions, even showing double peaks in [N II] (*right panels*).

[S II] lines. All velocities here are heliocentric. Results from our 1-g best fits are reported in Table A.1.

While the 2-g models can be considered in some sense better than the 1-g ones because of the smaller residuals, the corresponding best-fit parameters must be treated with caution. The blue and red best-fit radial velocities (RVs) of each modeled line were in most cases only a few km s^{-1} from one another, that is much closer together than the line widths (σ) themselves: this makes the relative intensities of the two Gaussian components much more uncertain than their total value, which was instead robustly modeled by 1-g fits (this is especially true of low S/N spectra). Therefore, the choice of considering one set of model parameters or the other will depend on the specific problem. We found that diagnostics involving two lines simultaneously (e.g., line-intensity ratios, or linewidths comparisons) were derived much more robustly from 1-g fitting parameters; on the other hand, the description of the gas dynamics considering RVs alone benefitted also from the 2-g model velocities, whenever S/N was sufficient. In this respect, we remark that the smaller thermal widths of the [N II] and [S II] lines permit often a more accurate derivation of components' RVs, despite these lines being weaker than Hα.

In several cases among those shown in Figs. 2 to 4, residuals from 1-g fits showed a blue component. This might be indicative of an approaching ionized layer, blueshifted with respect to the bulk of ionized gas, and reminiscent of the layer in the outer part of the Orion nebula, known as the Veil (see the reviews by O'Dell 2001; O'Dell et al. 2008). More detailed indications on the dynamics of the neutral gas probably associated with this layer in the M 8 nebula are derived from the sodium absorption lines in Sect. 3.2 below.

Some general properties of the ionized gas may be derived from the best-fit parameters. Figure 5a shows a comparison between RVs derived from 1-g fits to Hα and [N II] 6584 Å lines. The same pattern is shown by measurements from pure-sky fibres and from faint stars, confirming that the usage of faint-star spectra introduced no biases in the derived nebular properties. The datapoints scatter is not caused by errors (<1 km s^{-1} as a rule) but is real: in many cases the [N II] RV is less negative than the Hα RV. The velocity of the low-mass stars in the NGC 6530 cluster is $RV = 0.5 \pm 0.2$ km s^{-1} (Prisinzano et al. 2007), which

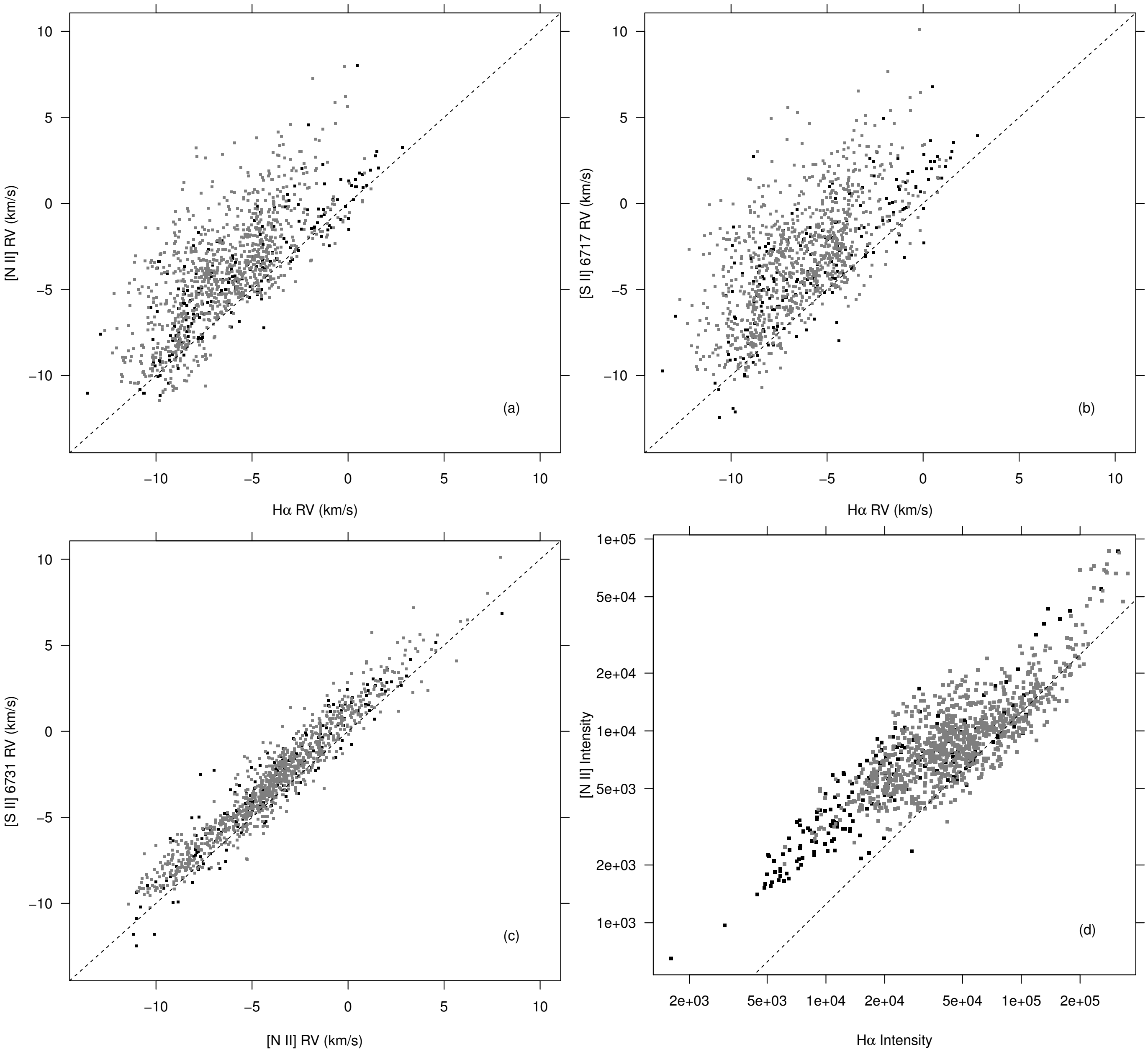

Fig. 5. *a)* Comparison between 1-g best-fit RVs from Hα and [N II] 6584 lines. Black dots indicate pure-sky fibres while gray dots indicate faint stars. The dashed line indicates identity. *b)* Same comparison as in *panel a*, between Hα and [S II] 6731. *c)* Same comparison as in *panel a*, between [N II] 6584 and [S II] 6731. *d)* Comparison between intensities of Hα and [N II] 6584, as resulting from 1-g models. Symbols as in *panel a*. The dashed line represents a ratio of 1/8.

was assumed to coincide with the center-of-mass velocity $RV_{\rm cm}$ of all cluster stars. The figure then shows than the bulk of ionized gas emitting in these lines has negative velocities (approaching us) from the standpoint of the cluster center of mass. This is unlike the case of the Carina nebula, where the double emission line peaks bracket usually the center-of-mass RV, indicating expansion toward both the near and far sides (Damiani et al. 2016). In NGC 6530, the ionized gas seems instead to expand predominantly toward our side (but more details will be studied in Sects. 3.3 and 3.4 below). Figure 5a however shows that along some sightlines the [N II] moves away from us, while hydrogen moves toward us: clearly, the different lines arise from dynamically distinct gas layers, a feature which cannot be understood from narrow-band images, which mix emission from all velocity layers (e.g., Tothill et al. 2008, Fig. 4). The comparison between Hα and [S II] RVs in Fig. 5b shows a pattern very similar to Fig. 5a. This suggests that the [N II] and [S II] lines originate from gas layers which are more closely related mutually than with Hα. This is confirmed by the good correlation shown in Fig. 5c, between the [N II] and [S II] RVs, the small systematic shifts being attributable to the uncertainty in the adopted line wavelengths[1]. This figure also permits to estimate empirically the maximum errors in the best-fit RVs from the scatter of datapoints in the correlation, on the order of $\leq$1 km s^{-1}. We remark that the [S II] and [N II] lines are the weakest being studied, the Hα line being much stronger; therefore, the scatter of datapoints in both Figs. 5a and b is certainly dominated by real effects.

---

[1] Wavelengths adopted here are 6583.43 Å for [N II], and 6716.44, 6730.815 Å for [S II], the latter two from Kaufman & Martin (1993).

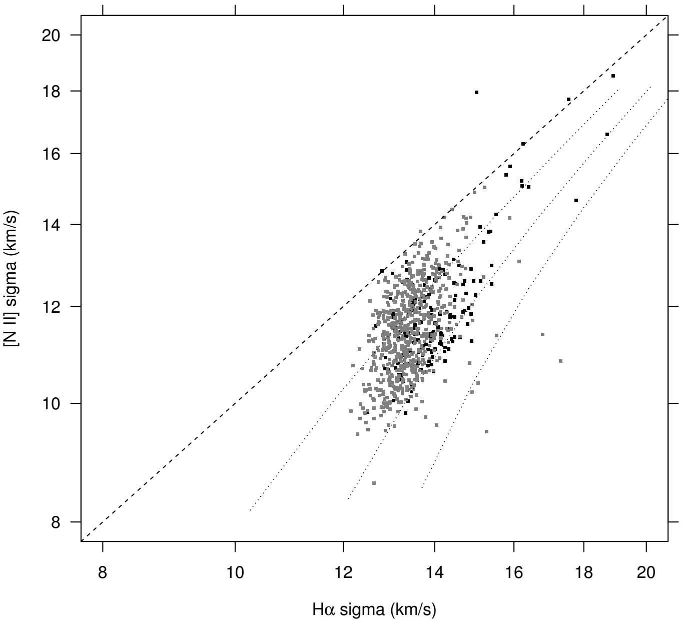

Fig. 6. Comparison between line widths σ of Hα and [N II] 6584, as resulting from 1-g models. Symbols as in Fig. 5. The dotted lines indicate loci of thermally broadened lines for $T = 5000$, 10 000, and 15 000 K, respectively from left to right. The dashed line represents identity.

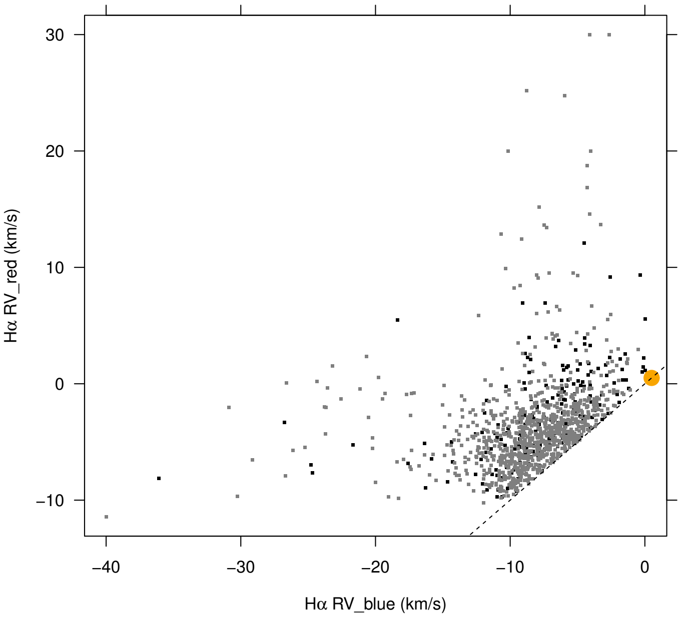

Fig. 7. Comparison between RV of blue and red components as resulting from 2-g model fits of the Hα line. Symbols as in Fig. 5. The orange circle indicates $RV_{\rm cm}$ of late-type cluster stars in NGC 6530, from Prisinzano et al. (2007).

The above results are reminiscent of those found in the Orion nebula, a well studied blister H$_{\rm II}$ region, where ionized gas flows away from the ionization front, and ionized hydrogen is found at more negative speeds with respect to [N II] and [S II], the ionization level gradually increasing as the gas acquires larger and larger speeds in a champagne-flow geometry (e.g., Balick et al. 1974; O'Dell et al. 1993). The analogy with the Orion nebula, although very interesting, cannot however be pushed too far, since there are also important differences between it and M 8: this latter is a much larger region, with more than one ionizing O-type star, and is probably also a more evolved blister, where at least the most massive star 9 Sgr has excavated a larger cavity in the parent cloud compared to that excavated by the Orion most massive member, θ^1 Ori C. We will examine in more detail the relative geometry of 9 Sgr and the M 8 nebula in Sect. 3.3.2.

A comparison between the 1-g model intensities of Hα and [N II] lines is shown in Fig. 5d. The intensity ratio is significantly non-uniform; this, under the typical conditions found in H$_{\rm II}$ regions, suggests significant differences in the ionization parameter across the region (e.g., Viironen et al. 2007), which will be studied in Sect. 3.3. In very general terms, in regions with high Lyman-continuum flux ionization will be highest, and hydrogen lines dominate over [N II] lines; in the same regions, the diagram suggests that the highest densities and largest surfact brightnesses are also found. In Sect. 3.3 we will examine in much better detail how these quantities depend on position across the nebula. Figure 6 shows the best-fit linewidths σ of Hα and [N II], whose comparison provides a measure of temperature (since turbulent and instrumental broadenings are the same for the two lines). To avoid mixing unrelated gaseous layers, we only showed datapoints having maximum absolute RV differences of 3 km s^{-1} between the two lines. In the figure, dotted lines indicate loci for fixed temperatures of 5000, 10 000, and 15 000 K, and a range of combined turbulent+instrumental broadening (between [8–18] km s^{-1}). Most datapoints lie between 5000–10 000 K, however with considerable spread.

We then examined the details of line profiles, as provided by our 2-g best-fit models. In Fig. 7 the RV of the blue component is compared with that of the respective red component in the same spectrum. Also these more detailed RVs show motions predominantly toward us (as seen from center of mass); only a small number of spectra showed blue and red RV components lying on opposite sides of $RV_{\rm cm}$ (i.e., $RV_{\rm red} > 0.5$ km s^{-1} and $RV_{\rm blue} < 0.5$ km s^{-1}), as it would be expected for an expansion originated from center of mass velocity. In the large majority of cases, the two components, both approaching us, have RVs differing by only few km s^{-1}, whose physical origin is not completely clear. One possibility is that the two components are actually an oversimplification of reality, and that they only represent the approximate RV range found in a rapidly decelerating layer emitting Hα. This accounts well for the significant correlation found in Fig. 7 between $RV_{\rm red}$ and $RV_{\rm blue}$ in the Hα line[2]. The median intensity of the blue component is only slightly higher than that of the red component (1.3 to 1.5 times, from pure-sky and faint-star fibres respectively), thus backscattering from dust is unlikely to account for the bulk of the red component.

Still different is the picture derived from the corresponding diagram involving the [N II] line (Fig. 8). Motion receding from us is much more frequently found, and the correlation between $RV_{\rm red}$ and $RV_{\rm blue}$ is much less tight, if existing at all. The blue and red components of [N II] are therefore in many cases indicative of dynamically distinct gas layers, whose spatial characteristics will be examined in detail in Sect. 3.3. It is interesting to compare the RVs for the Hα and [N II] lines, as given by the 2-g fits, analogously to the 1-g RV comparison of Fig. 5a. This was done in Fig. 9: here we see that, unlike the 1-g fit RVs, there is in most cases a fairly good match between RVs of the two lines, apart from a minority of strong outliers. In order to reconcile this

---

[2] Alternatively, this might be an instrumental effect arising from the non-Gaussianity of the line-spread-function, a systematic effect that becomes observable at the highest signal levels, see Damiani et al. (2016, Appendix).

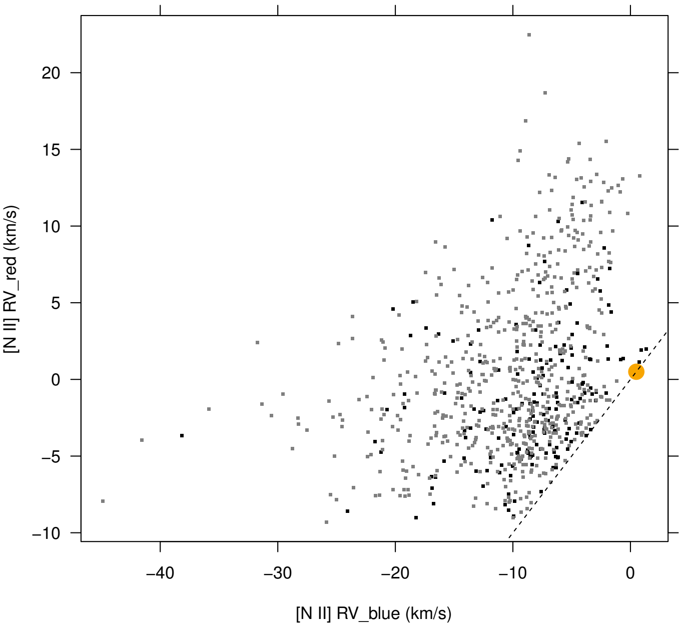

Fig. 8. Same as Fig. 7, for the [N II] line.

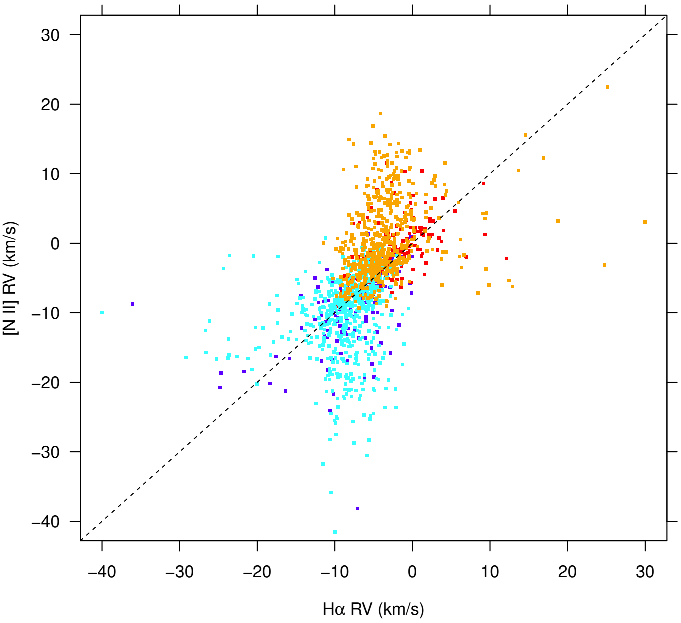

Fig. 9. Comparison between RVs of Hα and [N II] 2-g fits. The results of each individual spectrum are plotted twice, once for the red Hα and [N II] components, and again for the blue components of the same lines. Blue and red dots refer to blue and red components from sky fibres, while cyan and orange dots refer to the same components from faint stars.

agreement with the disagreement of 1-g RVs shown by Fig. 5a, one may expect that the relative intensities of the blue and red components are different between Hα and [N II], with the red component being dominant in [N II] over Hα, and viceversa for the blue component. This expectation is confirmed by the diagram of Fig. 10, where the intensities of the different lines were compared (for each blue and red component separately). Only components with an absolute RV difference less than 3 km s^{-1} were plotted. It is clear that red components tend to have a larger [N II]/Hα intensity ratio than blue components, and therefore lower ionization, as mentioned above. Recalling the above result that the two components are diagnosing different layers from gas moving in the same direction, we infer that the gas moving faster (larger negative velocities: blue component) is more ionized than the slower red component.

3.2. [O III] and sodium D lines from UVES data

A representative selection of line profiles of the [O III] 5007 Å line[3] from UVES spectra of several stars is shown in Figs. 11 and 12. Although all spectra are from stars and not sky fibres, the nebular line is clearly evident; no stellar spectrum subtraction was performed (apart from a constant continuum level) for any of the spectra shown. This line is frequently the second strongest nebular line in our spectra, after Hα. In the [O III] line doubly-peaked profiles are much more frequently found (as already reported by Elliot & Meaburn 1975) than in lower-ionization lines like those of [N II]. Even if no double peaks are found, line distortions are evidently present in most cases, and required 2-g fits. In only one case (labeled star 520-5, upper left panel in Fig. 12) two Gaussians provided a bad fit (as shown), and three components are suggested by the line profile: this is the O7 star Herschel 36 in the Hourglass nebula, having also the strongest [O III] line among our sample. Shown with green lines in Figs. 11 and 12 are our 2-g model fits, which reproduce the [O III] profiles very well, except for Herschel 36.

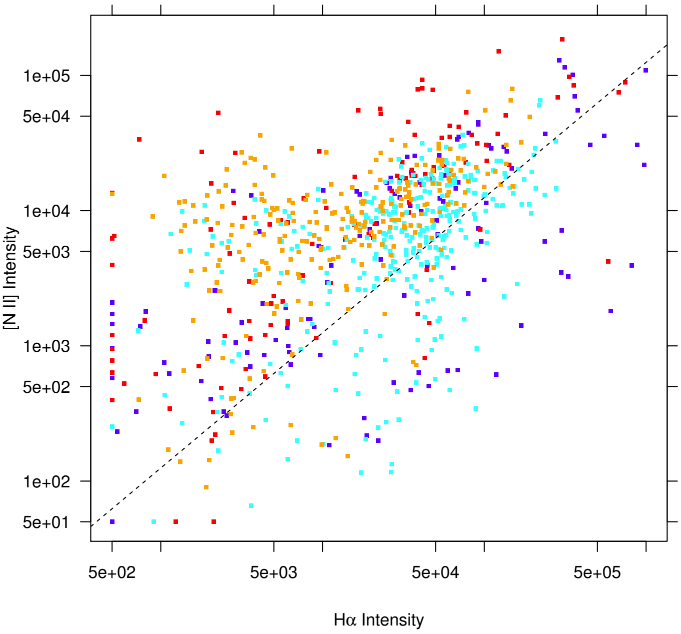

Fig. 10. Comparison between intensities of Hα and [N II] (log scales), from 2-g fits. Symbols as in Fig. 9.

The UVES spectra of stars in NGC 6530 also enabled us to study the neutral gas along the line of sight to these stars, using the sodium D doublet. The selection of UVES targets in the *Gaia*-ESO Survey was such as to maximize the probability of their cluster membership (Bragaglia et al., in prep.); therefore, most (not all) UVES spectra are likely to sample the entire column of neutral sodium between us and NGC 6530. A wide selection of sodium absorption line profiles for these stars is presented

---

[3] The exact wavelength used here is 5006.843 Å, from NIST (`http://physics.nist.gov/asd`, Kramida et al. 2015).

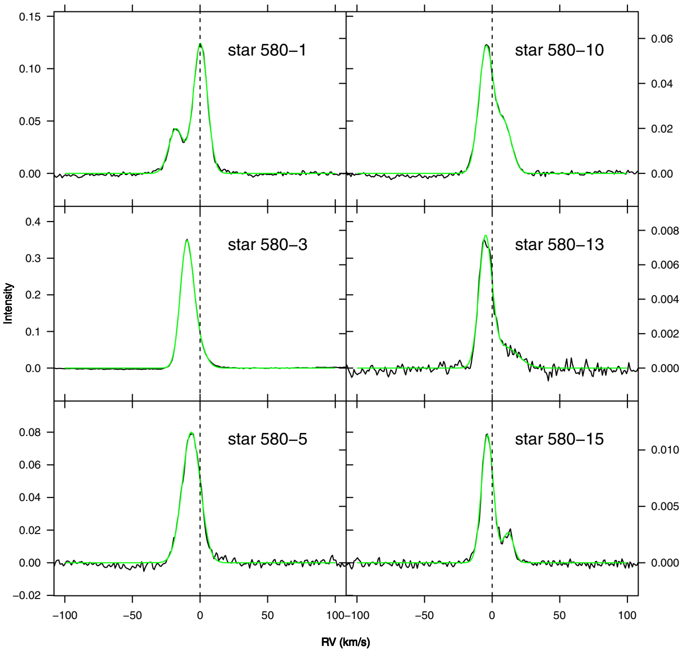

Fig. 11. Line profiles (black) and 2-g best-fit models (green) for the [O III] 5007 line, from UVES stellar spectra.

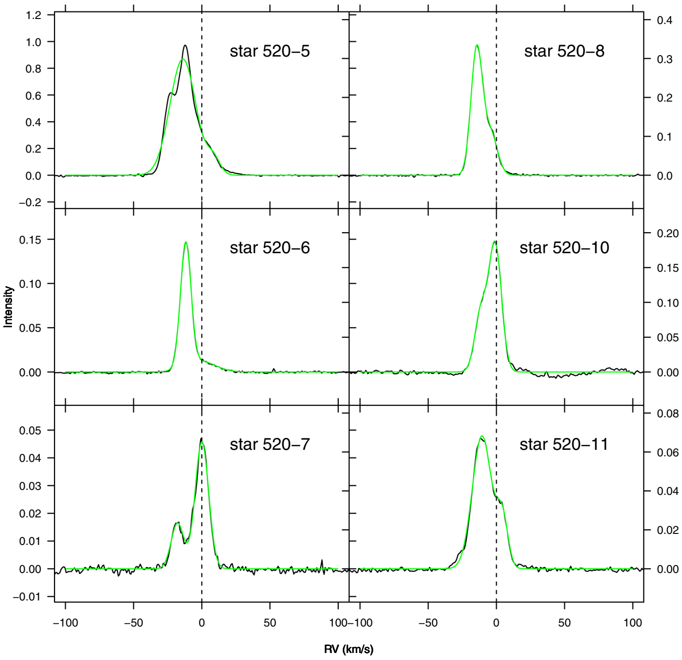

Fig. 12. Additional [O III] line examples, as in Fig. 11. Star 520-5 is the O star Her 36, the only case in which the two-Gaussian profile fails to match well the observed profile.

in Fig. 13. For not-too-hot stars, the stellar sodium lines were also evident in the spectra: these were divided out, using suitable template spectra chosen among the UVES-POP library (Bagnulo et al. 2003), such that Fig. 13 shows only non-stellar absorption components. Both doublet lines are shown, the D1 line in black, and the stronger D2 line in red. The occasional features at ~10 and 30 km s^{-1} in the D1 line (only) are telluric. The intensity ratios of the two lines are closely related, being originated from the same (ground) level, and having oscillator strengths of f_{D2} = 0.6405 (D2) and f_{D1} = 0.3199 (D1). The low ionization energy of sodium (5.139 eV) implies that these lines must originate from layers more distant from the OB stars (nearer to us) than the ionic lines studied in Sect. 3.1. In basically all cases, more than one absorbing layer, each with a distinct RV, is needed to model the sodium absorption profiles. The most complex line profiles are modeled with five Gaussians.

The fitting function was chosen as follows: we rewrite Eq. (1) from Hobbs (1974) using λ instead of ν as (for a single component)

$$N\frac{\pi e^2}{m_e c}\frac{\lambda^2}{c}f = N\int \alpha_\lambda \, \mathrm{d}\Delta\lambda = \int (-\ln r_\lambda)\, \mathrm{d}\lambda, \tag{1}$$

and the term containing the residual intensity r_λ, for a combination of absorbing layers i, as

$$\int (-\ln r_\lambda)\, \mathrm{d}\lambda = \sum_i N_i \int \frac{1}{\sqrt{2\pi}\sigma_i} \exp\left(-\frac{1}{2}\frac{(\lambda-\lambda_i)^2}{\sigma_i^2}\right) \mathrm{d}\lambda, \tag{2}$$

where $\lambda_i = \lambda_0 + v_i/c$ is the central wavelength of absorbing component i, at velocity v_i, and λ_0 is the line rest wavelength. σ_i is the component intrinsic width in wavelength units. The explicit form for r_λ is therefore:

$$r_\lambda = \exp\left(-\sum_i \frac{N_i}{\sqrt{2\pi}\sigma_i} \exp\left(-\frac{1}{2}\frac{(\lambda-\lambda_i)^2}{\sigma_i^2}\right)\right). \tag{3}$$

Since the lines from cold neutral sodium may be very narrow, and saturated absorption profiles may become highly non-Gaussian, the instrumental resolution of UVES was separately introduced as a fixed Gaussian broadening through convolution, and the final functional form used to fit the observed, normalized line profiles is:

$$r_\lambda^{\mathrm{obs}} = r_\lambda \otimes \int \frac{1}{\sqrt{2\pi}\sigma_{\mathrm{UVES}}} \exp\left(-\frac{1}{2}\frac{\Delta\lambda^2}{\sigma_{\mathrm{UVES}}^2}\right) \mathrm{d}\Delta\lambda, \tag{4}$$

where $\otimes$ is the convolution operator and σ_{UVES} (~2.7 km s^{-1}) is the UVES instrumental linewidth. The chosen function for r_λ corresponds to absorption from cold gas, whose emissivity is approximated as zero. Using this function, non-linear fits were attempted to the D2 line profiles (the strongest of the doublet) with two to five components; the optimal number of fitting components was determined by inspecting the results visually. The chosen best-fit models of D2 lines are superimposed to the observed profiles in Fig. 13 as orange curves: these match so well the observed profiles as to result often indistinguishable from them. Velocities of the individual best-fit components are indicated in the figure. They range from ~−50 km s^{-1} to ~+10 km s^{-1}; however, positive-velocity components were found only in two cases, the most evident example being that of star 520–14 in the figure. As it should be clear from Eq. (1), the profiles of the D1 line can be obtained from those of the D2 line (Eqs. (3) and (4)) by multiplying the intensity of each component N_i by the constant factor f_{D1}/f_{D2}. Model profiles of the D1 line obtained in this way are also shown in Fig. 13 as blue lines. In most cases, they match well the observed D1 profiles (black), providing a test of the goodness of the adopted best-fit models. Best-fit parameter values are reported in Table A.2. Intensity values $N_i > 1000$ correspond to saturated components and are highly uncertain.

However, a number of cases were found where the observed D1 profile and its model do not match (see e.g., stars 520-13, 520-14, 520-28, 520-36, 520-39), to a significant degree for the given S/N. The discrepancy occurs always near velocities of ~−30 to −20 km s^{-1}. It is always in the same sense, with the

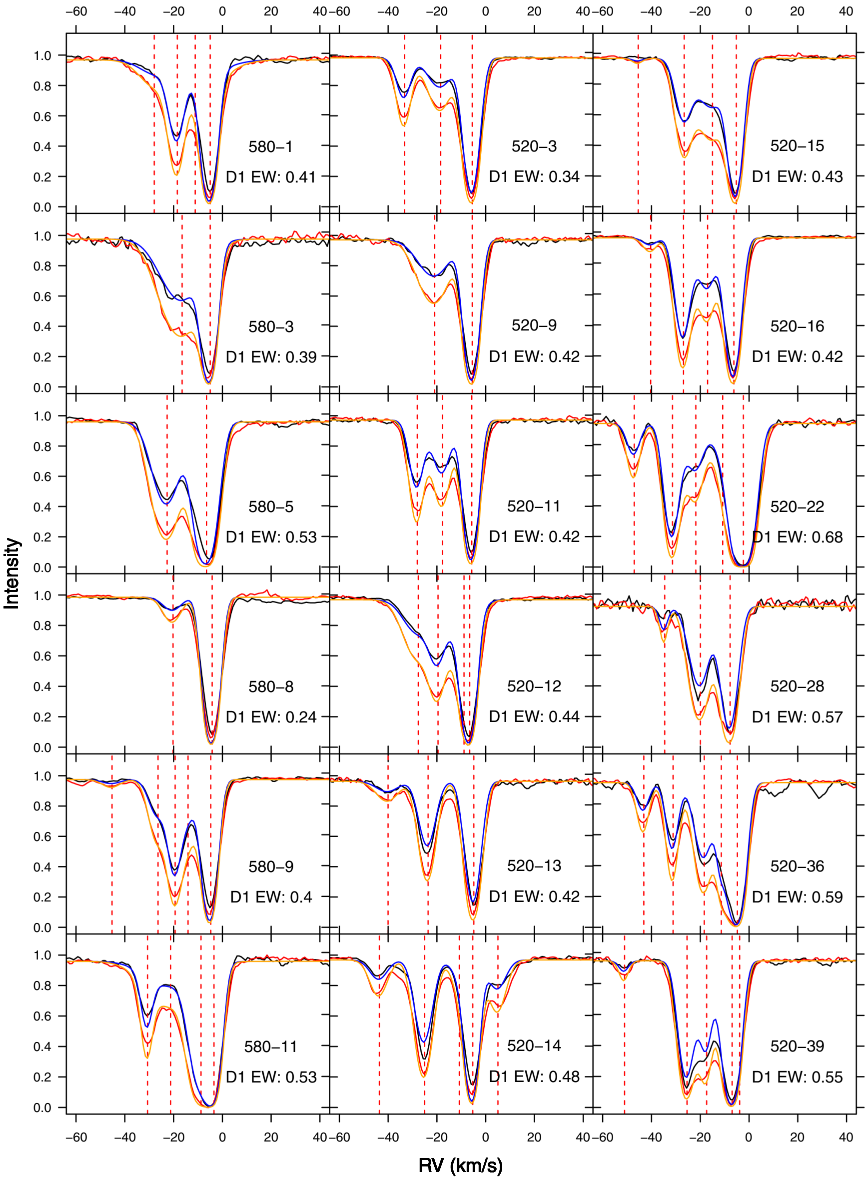

Fig. 13. Profiles of interstellar sodium D1 (black) and D2 (red) lines from UVES spectra (both setups 580 and 520, as labeled). The stellar line contributions, when present, were removed by division with suitable template spectra. The orange curves are multiple-Gaussian best-fit models to the D2 profiles; the blue curves are D1 profile predictions based on the D2 models, and assuming pure absorption (see text). Vertical red dashed lines indicate the best-fit RVs of model components. Total equivalent widths for the D1 lines are also indicated (in Angstroms).

observed D1 profile being deeper and closer to the respective D2 profile than the model would predict: this is suggestive of that particular component saturating toward a finite, non-zero intensity, contrary to the assumption above of zero emissivity. If this latter condition is not met, the profile modeling becomes extremely more complex, the contributions from different layers not being writable as a linear sum in $\ln r_\lambda$; also the order of layers along the line of sight becomes important (the emission of one layer can be absorbed only by the layers closer to us), which is not the case when pure absorption is modeled. We have therefore not modeled those few cases in quantitative detail. Qualitatively, it is suggested that the layers at velocities ~ -30 to -20 km s^{-1} are sometimes hotter than those at lower and higher velocities, their source function being much higher than zero compared to the photospheres of the UVES targets. Temperatures of several thousands K are therefore likely for those particular sodium layers. We consider it likely that these layers are spatially adjacent to those where recombination has recently taken place, as also supported by their similar velocities. The higher temperatures in the sodium layers at ~ -30 to -20 km s^{-1} are also supported by their increased line widths σ, as shown by Fig. 14. We remark that this figure shows intrinsic line widths σ_i, not the observed values, degraded by the instrumental resolution (as in Eq. (4)). For this reason, their lower bound was set to zero in the fitting; however, values of σ_i lower than ~ 3 km s^{-1} should be regarded as upper limits.

The wide variety of absorption profiles found within small angular scales on the sky suggests strongly that the associated neutral gas lies in the immediate vicinity of the Lagoon nebula, and not all along the line of sight. Also the observed large radial velocities of sodium absorption are not expected for the general ISM gas in nearly circular orbits and observed almost in the direction of Galactic center, and further support this argument. The same cannot be said for the strong, saturated component near ~ -5 km s^{-1}, which although not strictly identical in all profiles is so widespread (and consistently narrow) that we cannot rule out a line-of-sight origin. A puzzling feature from the sodium spectra is the clear existence of components at much larger negative velocities than found from the ionic lines in Sect. 3.1: at face value, this would imply that the expanding gas, after recombining at a typical approaching velocity of -5 to -10 km s^{-1} (Fig. 5a), keeps accelerating toward us to produce the neutral layers around -30 to -40 km s^{-1}. Also the origin of the discrete velocity components (as opposed to a continuous velocity

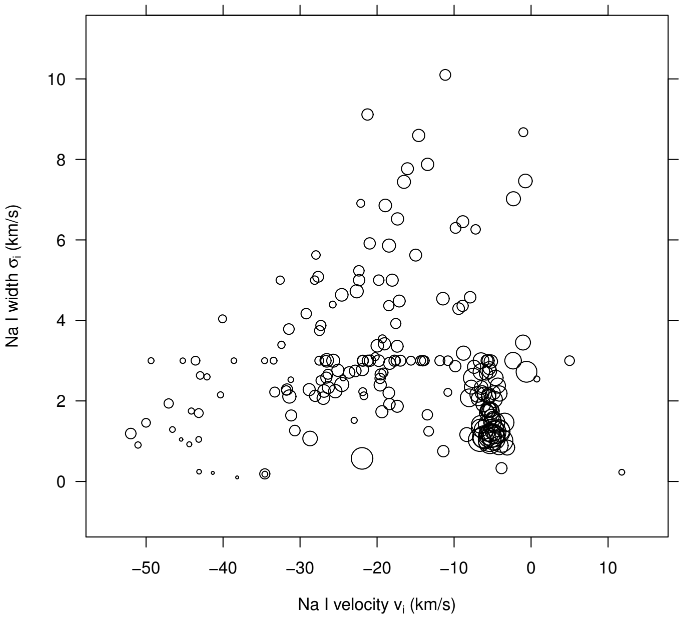

Fig. 14. Sodium absorption linewidths σ_i vs. radial velocities v_i, for all fit components. Circle size is proportional to component intensity.

distribution) in the sodium profiles is unclear, that is whether it is related to a episodic energy input or to different pre-existing layers of neutral gas, swept by the expanding envelope. In the former case, a single star would be driving the phenomenon, or otherwise the uncorrelated input from many stars would produce a smoother velocity distribution. In the second, a continuously (non-episodically) expanding shell would encounter discrete gas layers, and decelerate as more and more mass is being pushed; this seems contradictory with the above suggestion that neutral gas is accelerated outwards, in the sodium-line formation region.

We have also computed equivalent widths for the D1 line (labeled D1 EW in Fig. 13), which fall in the range 0.4–0.6 Å for the bulk of stars. Using the relation given by Munari & Zwitter (1997), this range would imply a $E(B-V)$ range of 0.2–0.5, in good agreement with that found by Sung et al. (2000) for the NGC 6530 massive stars.

3.3. Spatial maps

Most of the properties characterizing the nebular emission, as derived from the line modelization discussed in Sect. 3.1, show distinct spatial patterns, which we examine in detail here. Figure 15a shows a map of the [N II]/Hα intensity ratio (proportional to symbol size), superimposed on a VPHAS+ image of the nebula as in Fig. 1. As mentioned in Sect. 3.1, a smaller intensity ratio corresponds to higher ionization parameter. While one would expect the latter to increase in the vicinity of the hottest stars, this is not always found in our data. Not considering the two O stars near the east (HD 165246) and west (HD 164536) edges of the nebula, where our spatial coverage is sparse, we observe a clear ionization increase around HD 165052 (in south-east region), while the bright nebula surrounding the Hourglass shows no clear ionization pattern around its three O stars (north to south: HD 164816, 9 Sgr, and Herschel 36). The darker nebula parts (called the Great Rift in Lada et al. 1976) around this brightest region shows distinctly higher ionization than near the Hourglass. The relatively low ionization near 9 Sgr supports further the suggestion by Lada et al. (1976) that this star should lie several pc in front of the nebular material, not in its immediate vicinity. The irregular ionization near Herschel 36, instead, can be attributed to the patchy distribution of dense gas and dust all around this star, as suggested by the HST image of the Hourglass (Tothill et al. 2008). Near the central NGC 6530 cluster, to the S-E of the Great Rift, ionization is often higher than in the Hourglass region; however, there seems to be a gradient across the cluster, not a peak near its center, so that the source of ionization is probably not internal to the cluster, with the best candidate remaining the O4 star 9 Sgr, despite being a few parsecs away. The issue will be examined in more detail in Sect. 3.3.2 below. The bright blue supergiant HD 164865 (B9Iab) probably contributes to ionization locally, but not predominantly since there is no associated ionization peak near it.

We next considered the nebular electron density, as measured from the ratio of [S II] 6717, 6731 Å lines (Fig. 15b). The spatial pattern is here very different than the ionization pattern: a strong and distinct increase in density ($\sim 3000 \times \sqrt{10^4/T}$ cm^{-3}, in agreement with Bohuski 1973) is found throughout the vicinity of the Hourglass, with the peak coinciding with the Hourglass proper. The agreement between line ratios from pure-sky fibres and faint-star spectra is very good, which is especially crucial here because of the near coincidence between the [S II] 6717 line and a Ca I photospheric line. A very localized enhancement in density is also found in the immediate vicinity of the bright rim near M 8E-IR (S-E of NGC 6530). Near the stellar cluster core, instead, the density is not particularly high ($\sim 800 \times \sqrt{10^4/T}$ cm^{-3}), not higher than in the neighboring Great Rift, despite the large difference in nebular brightness. The density decreases very smoothly toward the nebula edges, to $\sim 50 \times \sqrt{10^4/T}$ cm^{-3}. The density was derived from the doublet ratio using analytic expressions in Weedman (1968) and Saraph & Seaton (1970).

The radial velocity map for Hα, shown in Fig. 16 provides a vast amount of information. Velocities are here those derived from 1-g fits. Since $RV_{\rm cm} \sim 0$, absolute velocities are nearly the same as $|RV - RV_{\rm cm}|$, that is referred to the NGC 6530 center of mass. There is no central symmetry in the velocity field. The cluster core nearly coincides with a (negative) velocity maximum: absolute velocities decrease toward both S-E and N-W from this position. The location of these low-absolute-velocity datapoints defines a reference direction, indicated with a red arrow in the figure; this is almost coincident with the normal to the galactic plane. The galactic plane itself is just off the figure region to the right. The Hourglass region is also characterized by large negative velocities, but no velocity minimum is detected west of it, probably also because of the incomplete spatial coverage. In the outermost nebula regions to the east the velocity smoothly decreases toward $RV_{\rm cm}$. However, this does not happen in the western edge, where velocities remain at large negative values, a surprising fact which will be discussed in more depth in Sect. 3.4.3.

The velocity map obtained from the 1-g [N II] line fits is instead shown in Fig. 17: although it presents many similarities to the analogous map for Hα of Fig. 16, there are also important differences: in the Hourglass region the negative velocity maximum is much less pronounced; on the contrary, in the Great Rift even positive velocities are found. That is, the Hα and the [N II] lines in this region indicate gas moving in opposite directions with respect to the cluster center-of-mass velocity $RV_{\rm cm} = 0.5$ km s^{-1}. In the N-W part, the puzzling large negative velocities are again found.

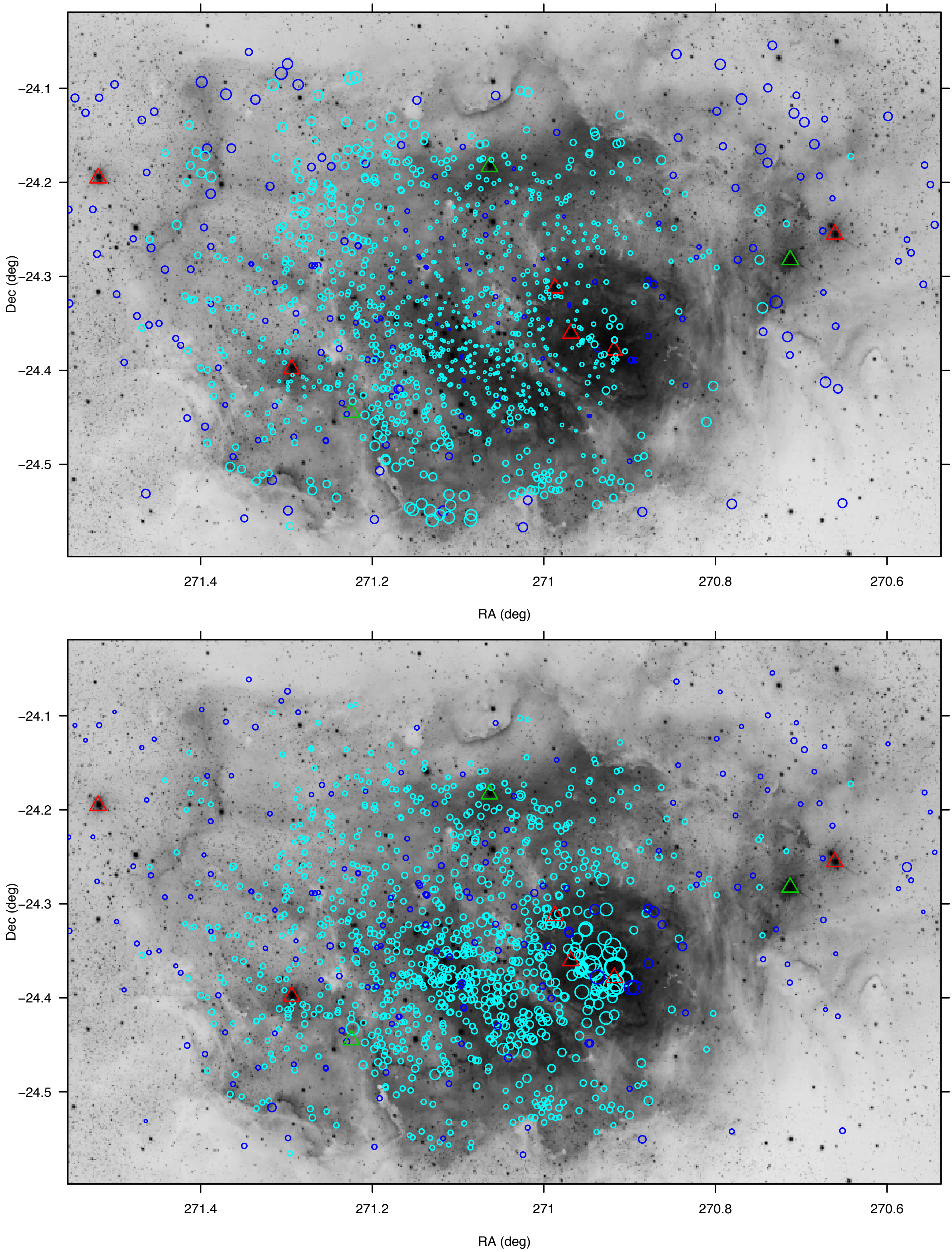

Fig. 15. *a)* (*Upper panel*) map of intensity ratio between [N II] and Hα (proportional to circle size) from 1-g model fits, superimposed to the same VPHAS+ image as in Fig. 1. Blue (cyan) circles refer to pure-sky (faint star) fibres. Triangles have the same meaning as in Fig. 1. *b)* (*Lower panel*) map of [S II] 6731/6717 intensity ratio (proportional to circle size, and increasing with density). Symbols as in *panel a*.